MATERIALS SCIENCE

When and how self-cleaning of superhydrophobic surfaces works

Florian Geyer[1], Maria D'Acunzi[1], Azadeh Sharifi-Aghili[1], Alexander Saal[1], Nan Gao[1,2]*, Anke Kaltbeitzel[1], Tim-Frederik Sloot[3], Rüdiger Berger[1], Hans-Jürgen Butt[1†], Doris Vollmer[1†]

Despite the enormous interest in superhydrophobicity for self-cleaning, a clear picture of contaminant removal is missing, in particular, on a single-particle level. Here, we monitor the removal of individual contaminant particles on the micrometer scale by confocal microscopy. We correlate this space- and time-resolved information with measurements of the friction force. The balance of capillary and adhesion force between the drop and the contamination on the substrate determines the friction force of drops during self-cleaning. These friction forces are in the range of micro-Newtons. We show that hydrophilic and hydrophobic particles hardly influence superhydrophobicity provided that the particle size exceeds the pore size or the thickness of the contamination falls below the height of the protrusions. These detailed insights into self-cleaning allow the rational design of superhydrophobic surfaces that resist contamination as demonstrated by outdoor environmental (>200 days) and industrial standardized contamination experiments.

INTRODUCTION

Surfaces exposed to the ambient atmosphere are contaminated by particulate matter over time. Particulate matter originates from nature (e.g., microorganisms and pollen) or is man-made, such as soot from combustion (*1*). This makes easy cleaning or, rather, self-cleaning desirable. Self-cleaning is one of the most prominent features of superhydrophobic surfaces. Although almost 2000 articles were published on superhydrophobicity in 2018 alone, it is still unclear how self-cleaning works in detail and which forces are involved in the process. To obtain a comprehensive understanding, it is important to visualize how the self-cleaning process evolves on the micrometer scale. The resistance of superhydrophobic surfaces to particulate matter and nanosized contamination is inevitable for the use of these surfaces for a variety of real-world applications. Apart from self-cleaning (*2*), for instance, this is essential for the development of waterproof textiles (*3*, *4*), antibiofouling surfaces (*5*–*7*), drag reduction (*8*, *9*), anti-icing (*10*, *11*), membranes for gas exchange (*12*, *13*), oil/water separation (*4*, *14*), membrane distillation (*15*, *16*), or fog harvesting (*17*, *18*). Thus, the need for clear design principles on how to construct surfaces to resist particle contamination should be addressed (Fig. 1).

On superhydrophobic surfaces, water drops assume an almost spherical shape (contact angle, $\theta > 150°$) and easily roll off when the surface is tilted by a few degrees (<10°) (*19*). To achieve superhydrophobicity, the surface has to be coated by hydrophobic nano- or micrometer-sized protrusions. The protrusions need to be such that air is entrapped underneath, leading to the so-called Cassie state (*20*). This results in low adhesion of drops to the surface. Macroscopic contamination can easily be removed by rinsing with water drops, e.g., during rain or artificial showers (*21*).

Previous contamination studies focused on the influence of millimeter- to micrometer-sized contaminants on the performance of superhydrophobic surfaces, such as hydrophobic powder (*21*), micrometer-sized particulates (*22*–*24*), and aggregated bioparticles (*25*). Here, it is difficult to identify the influence of the individual particle size, as those particles were either comparatively large or aggregated as a powder. It is important to clarify how the deposition method, the particle size–to–pore ratio, and the particle polarity influence the resistance of the superhydrophobic surfaces to contamination. Drops were imaged from the side or top using optical photography or video microscopy while rolling over contaminated surfaces. Because of the high contact angle and the high depth of field, optical photography or video microscopy cannot provide detailed insight of the region close to the three-phase contact line (*26*), i.e., of the region where the drop, the contamination, and the superhydrophobic surface meet (see note S1). Thus, these methods do not provide information on how contamination is taken up, knowledge that is required for a microscopic understanding of self-cleaning. Furthermore, surfaces are usually cleaned at a predefined inclination, drop impact pressure, or velocity. This does not provide information about the forces individual droplets experience. The lateral adhesion and friction force a drop experiences while cleaning a contaminated surface have never been reported.

Here, we demonstrate that the removal of single particles can be investigated in a space- and time-resolved manner by using laser scanning confocal microscopy (LSCM). We visualize and quantify the forces involved in the self-cleaning process. A theoretical model of the friction forces is developed, which fits the measured forces and provides an understanding of the underlying processes. To design superhydrophobic surfaces that are resistant to hydrophobic and hydrophilic particle contamination, we found that the pore size of the superhydrophobic surface determines the lower size limit of the contaminant. Last, we demonstrate that superhydrophobic surfaces having a nanoscale pore size are capable of resisting long-term real-world exposure and industrial contamination tests.

RESULTS AND DISCUSSION

Model nanoporous surface

As an example of a superhydrophobic nanoporous surface, glass slides were coated with silicone nanofilaments (*7*, *27*, *28*). Briefly, the glass slides were immersed in a mixture of toluene with a certain water

[1]Max Planck Institute for Polymer Research, Ackermannweg 10, 55128 Mainz, Germany. [2]Future Industries Institute, University of South Australia, Mawson Lake Campus, South Australia 5095, Australia. [3]Evonik Resource Efficiency GmbH, Goldschmidtstraße 100, 45127 Essen, Germany.
*Present address: Department of Mechanical Engineering, University of Birmingham, Edgbaston, Birmingham B15 2TT, UK.
†Corresponding author. Email: butt@mpip-mainz.mpg.de (H.-J.B.); vollmerd@mpip-mainz.mpg.de (D.V.)

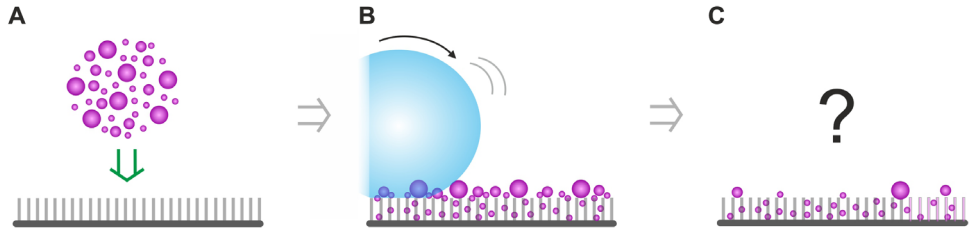

Fig. 1. Self-cleaning of superhydrophobic surfaces. (**A**) The surfaces are contaminated with particles of different sizes (80 nm to 50 μm) and polarities (hydrophobic/hydrophilic). (**B**) Water drops roll over the contaminated surface. (**C**) Can the water drops remove the contamination and how is superhydrophobicity affected? How does the self-cleaning evolve on the micrometer scale, and which forces are involved in the self-cleaning process?

content and trichloromethylsilane (TCMS). After a reaction time of 6 hours, the glass slides were covered by a 1- to 2-μm-thick layer of nanofilaments with diameters between 20 and 50 nm and spacings between 50 and 500 nm. To reduce the surface energy, we fluorinated the coated slides using a perfluoro silane. These surfaces show a high static water contact angle of 161° ± 4° and low roll-off angles of ≈1° for 6-μl water drops.

Model particles mimicking contamination

Spherical, fluorescently labeled, hydrophilic and hydrophobic particles were used to mimic different types of atmospheric particle contaminants. Our particles cover a size range from 80 nm to 50 μm and were made of silica nanoparticles of average diameters $2R = 84 \pm 9$ nm (denoted as 80-nm particles), 210 ± 30 nm (200-nm particles), and 580 ± 120 nm (600-nm particles); silica-coated polystyrene particles of $2R = 1.45 \pm 0.14$ μm (1.5-μm particles); and silica-coated glass beads of 32 ± 7 μm (10- to 50-μm particles). Scanning electron microscopy (SEM) images of these particles are provided in the Supplementary Materials (fig. S1). Without further treatment, the particles were hydrophilic and dispersed in ethanol. To vary inherent wetting properties, we hydrophobized a portion of the previously mentioned particles using octyl silane.

Hydrophobic particle powders

To mimic common hydrophobic contamination sources, such as soot or dust, we applied hydrophobic particle powders to the nanoporous superhydrophobic surfaces (Fig. 2, A and B). After contaminating the surfaces with the particle powder, the surfaces were cleaned by rinsing with 20 to 50 water drops of 16 ± 1 μl. These drops rolled off the inclined surfaces and took away the particles.

We found that hydrophobic powder contaminants (purple) could be effectively removed from the superhydrophobic surfaces (blue) as verified by LSCM (Fig. 2, C to E, and fig. S2). SEM analysis confirmed the results. Hardly any contamination could be found within or on top of the coating for all particle sizes [see Fig. 2 (C to E) and fig. S3 for more details of the sample contaminated with 80-nm particles]. The excellent self-cleaning is corroborated by low roll-off (<2°) and high contact angles (>150°; Fig. 2, F and G). Even after five consecutive contamination steps by particles of all different sizes followed by subsequent self-cleaning, the roll-off angles remained at 1° ± 1°, and the static contact angle at 161° ± 4°. Thus, even nanoscopic hydrophobic particle powders did not affect the superhydrophobicity of the nanofilament-coated surfaces.

Hydrophilic particles from a wetting dispersion

Particulates such as water-soluble organic carbon (WSOC) are hydrophilic, can disperse in water, and can, thus, stick much better to surfaces (*1*, *29*, *30*). To investigate the most severe case of contamination, we applied hydrophilic particles dispersed in ethanol to the nanoporous surfaces (Fig. 3). Fifty microliters of the particle dispersions with a concentration of ≈10 g liter^{-1} were cast onto the surfaces by a pipette. The dispersion wetted the surface and, lastly, completely dried out on the surface. Here, three cases of particle sizes can be distinguished:

i) The particle diameter $2R$ is larger than the pore diameter p (with $p < 2R$), and the particles cannot enter the coating (Fig. 3A). The 10- to 50-μm and 1.5-μm particles (Fig. 3C and fig. S4) fall in this category. In this case, the first water drop was able to remove most of the contamination. After the contaminants were removed, the contact angles stayed above 150°, and the roll-off angles remained below 2° (Fig. 3, F and G).

ii) The particle diameter is similar in size to the largest pores ($p \approx 2R$). The 600-nm particles were slightly larger than the largest pore diameter of the nanoporous coating but in a similar size range. Even in this case, for thin contamination layers (one to two loose particle layers), most particles could be removed. We only found some sparsely distributed particles and particle aggregates using LSCM and SEM (Fig. 3D and figs. S5 and S6, A and B). These remaining particles did not change the wetting properties (Fig. 3, F and G). Only in the case of a thick aggregated contamination layer, the self-cleaning of the surface failed. In particular, areas of up to 10-μm-thick contamination were found on the edge of the contamination spot because of the coffee stain effect during drying (*31*). The particles showed a high order in these areas and formed hydrophilic polycrystalline domains of ≈10 to 20 particle layers (fig. S6, C to E). On the coffee stain ring of the dried sample, the droplets stuck to the surface, and the roll-off angle increased to 90°.

iii) The particle diameter is smaller than the pore size ($p > 2R$), and the particles can enter the coating (Fig. 3B). Here, the 80- and 200-nm particles could enter and dry out within the pores (see Fig. 3E and fig. S7 for details). Even after rinsing, strong fluorescence of the nanoparticles could be observed within the coating (Fig. 3E and fig. S4). Hydrophilic 80- and 200-nm particles led to the failure of superhydrophobicity. The contact angles decreased to ≈140° and ≈40° for the 200- and 80-nm particles, respectively, and the roll-off angles increased above 90° for both. The droplets contacted the hydrophilic particles inside of the coating, wetting the hydrophilic particle patches (fig. S8). Therefore, locally, the Cassie state broke down, and the drops got pinned on the surface, being unable to clean the surface.

In contrast to the 80- and 200-nm hydrophobic particle powders that were littered over the surface, the hydrophilic counterpart particles were applied from a dispersion. To examine whether the way how we applied the particles to the surfaces caused the different influence of the particles, we performed additional experiments. We contaminated the surfaces with powders of hydrophilic particles with diameters of 80 and 200 nm. In this case, the roll-off angles of 6-μl drops stayed at 2° ± 1° and 2° ± 1° for the 80- and 200-nm particles, respectively. Thus, aggregated

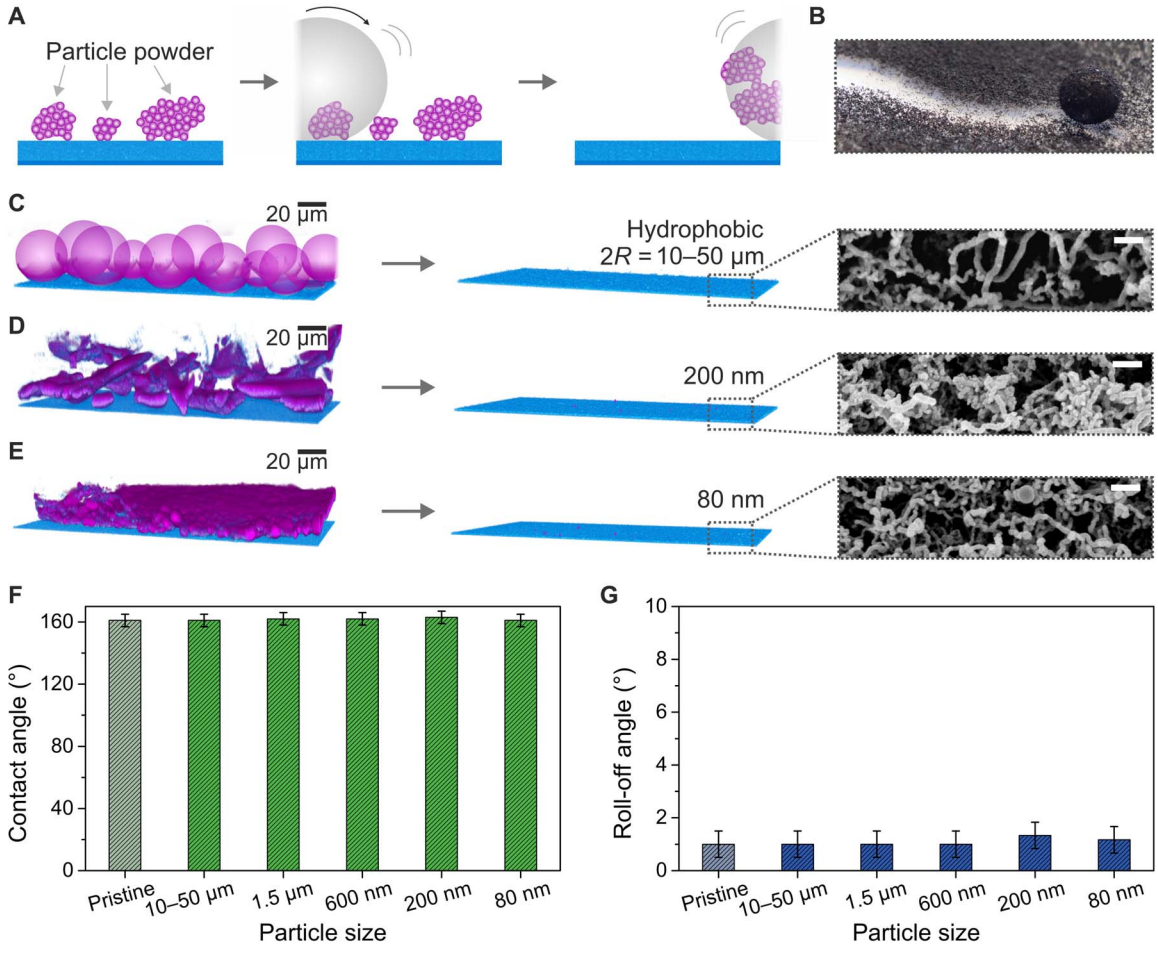

Fig. 2. Effect of differently sized hydrophobic particle powder contamination on nanoporous superhydrophobic surfaces. (**A**) Schematic illustration of the self-cleaning process of hydrophobic particle powders (purple) by a water drop (gray) on a superhydrophobic surface (blue). Colors and texture were chosen to match the LSCM images. (**B**) Photograph of a 10-µl water drop cleaning a nanoporous superhydrophobic surface contaminated with Oil Red dye particles (appear black). (**C** to **E**) LSCM images after contaminating the nanoporous superhydrophobic surface (left) with powders of hydrophobic particles with diameters of 10 to 50 µm, 200 nm, and 80 nm (see Materials and Methods for details of the image processing). Efficient cleaning of all hydrophobic powders was verified by LSCM (center) and SEM (right). Scale bars, 200 nm (SEM). (**F** and **G**) Contact and roll-off angles using 6-µl water drops after self-cleaning of a nanoporous surface consecutively contaminated with hydrophobic particle powders.

particle powders independent of particle size and hydrophobicity hardly affect the superhydrophobicity of the nanoporous surfaces. Next, we applied the 80- and 200-nm hydrophobic particles from dispersion in *n*-hexane. Now, the roll-off angles of 6-µl water drops slightly increased to 8° ± 6° and 20° ± 15° for the 200- and 80-nm particles, respectively. The large scatter of the roll-off angles indicates large local differences in particle contaminations.

Hence, independent of the hydrophobicity/hydrophilicity of the particles, only smaller particles ($p < 2R$) that are dispersed in a liquid capable of wetting the surface affect the self-cleaning and superhydrophobic properties. In particular, small hydrophilic particles are detrimental to the surface and can lead to a failure of self-cleaning. Consequently, to design superhydrophobic surfaces that are resistant to hydrophilic and hydrophobic particle contamination, the pore size needs to be below the lowest expected particle size ($p < 2R$). However, there is another important aspect that needs to be considered: the particle-particle interaction per volume. It depends on the radius, roughness, polarity, polydispersity, and order of the particles. During drying, the particles formed polycrystalline domains at the rim of the contamination spot (coffee stain effect), increasing the number of particle-particle contacts. The number of contacts also increases with decreasing particle size by $(R_1/R_2)^3$, where R_1 and R_2 refer to the radius of the larger and smaller particles. Thus, the interparticle interactions increased for the smaller particles of categories (ii) and (iii) compared with the particles of category (i). In addition, the thickness of the contamination layer can play an important role. In analogy to the thin plate theory, the stiffness of the particle layer is expected to increase with the third power of the layer thickness (*32*). Therefore, thicker films cannot be easily bent and need to be lifted off as a whole. During evaporation, impurities on the surface and in the dispersion concentrate in the contact zone of neighboring particles. This increases the contact area between particles and between the substrate and the particles, further enhancing the particle-particle and particle-surface adhesion. Therefore, in the case of the thick aggregated layer of hydrophilic 600-nm particles, the particles could not be easily removed from the surface.

Microstructured surfaces

Many superhydrophobic surfaces rely on microstructures (*33*). As a model, we investigated microstructured superhydrophobic surfaces that were made of SU-8 micropillars (rectangular, 10-µm height

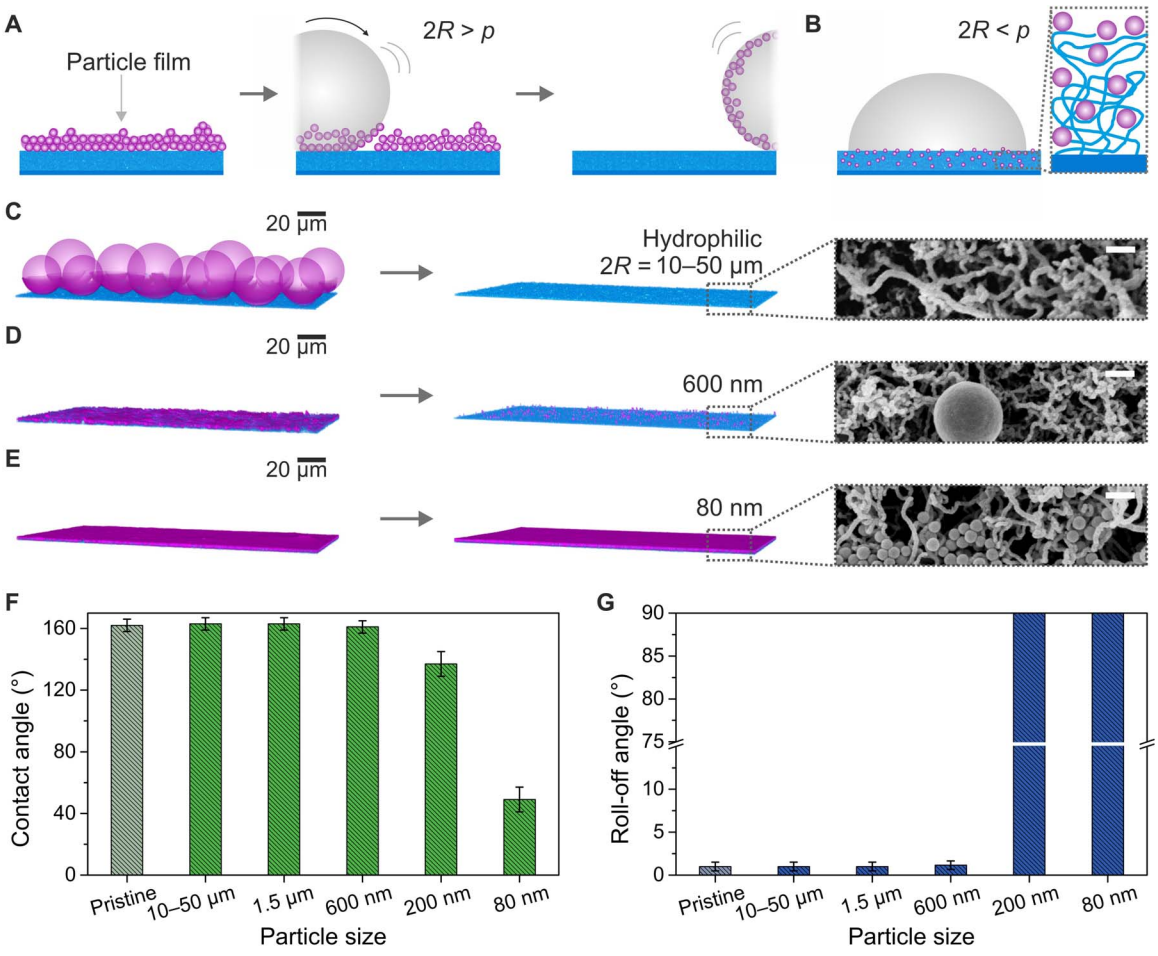

Fig. 3. Effect of hydrophilic particle contamination having various particle sizes deposited from ethanol dispersion on nanoporous superhydrophobic surfaces. (**A**) Schematic illustration of the self-cleaning process of hydrophilic particles (purple; $2R > p$) deposited from ethanol dispersion by a water drop (gray). (**B**) Particles of smaller diameter than the pore diameter ($2R < p$) can penetrate the coating (blue), affecting wetting properties. (**C** to **E**) LSCM images (left) after contamination of the superhydrophobic surfaces with hydrophilic particles with diameters of 10 to 50 µm, 600 nm, and 80 nm (see Materials and Methods and fig. S9 for details of image processing). LSCM (center) and SEM images (right) show the surfaces after rinsing. Scale bars, 200 nm (SEM). (**F** and **G**) Contact and roll-off angles using 6-µl water drops after self-cleaning of nanoporous surfaces contaminated with various hydrophilic particles (dried from ethanol dispersion).

with 5 × 5–µm^2 top areas; center-center distance of pillars, 20 µm) on glass slides using photolithography. The SU-8 micropillar surfaces were fluorinated and showed a static contact angle of 154° ± 4° and roll-off angles of 9° to 10° for 6-µl water drops. The superhydrophobic microstructured surfaces were exposed to hydrophilic 10- to 50-µm and 1.5-µm particles dispersed in ethanol (Fig. 4 and fig. S10, A to C). We found that water drops could easily remove the 10- to 50-µm particles. The 1.5-µm particles were stuck between the micropillars since $p > 2R$ (Fig. 4A). However, whether this causes degradation of the surface depends on the filling height of the contaminants h_c compared with the pillar's height h_P. If the particles only partially fill up the space between the pillars ($h_c < h_P$), then the superhydrophobicity will remain intact (Fig. 4B) because the drop only rests on the top faces of the pillars (fig. S10, D and E). If the coating is filled up or covered with particles ($h_c \geq h_P$), then superhydrophobicity will break down. This emphasizes the need for a small pore size to prevent small particles from penetrating the coating. Exposing a surface to hydrophobic particle powders led to decreasing roll-off angles with each contamination step (Fig. 4B). The reason is that residual particles of the powders remained on the surface, especially on the pillars' top faces (fig. S11). These particles add a second scale of roughness to the surface and, thus, yield a hierarchical nano/microstructured surface. Therefore, nanoscopic hydrophobic contamination can even reduce the roll-off angles of the coating.

Imaging self-cleaning on the microscale

However, while the ability to withstand various kinds of contamination is essential, the ease of self-cleaning is equally crucial. How are individual particles removed from the surfaces by single drops, and how large are the involved forces? To image the pickup process of particles, we modified a confocal microscope with a stage holding a needle. This setup allowed us to move drops over the surfaces during imaging. We investigated the self-cleaning process of hydrophilic 10- to 50-µm particles deposited on a nanoporous superhydrophobic surface using 10-µl drops (Fig. 5A and movie S1; particle fluorescence, purple; drop fluorescence, navy blue; and reflections, light blue). Confocal microscopy enabled us to measure the local contact angle on the surface of the micrometer sized particles (Fig. 5, B and C). When the drop was moved

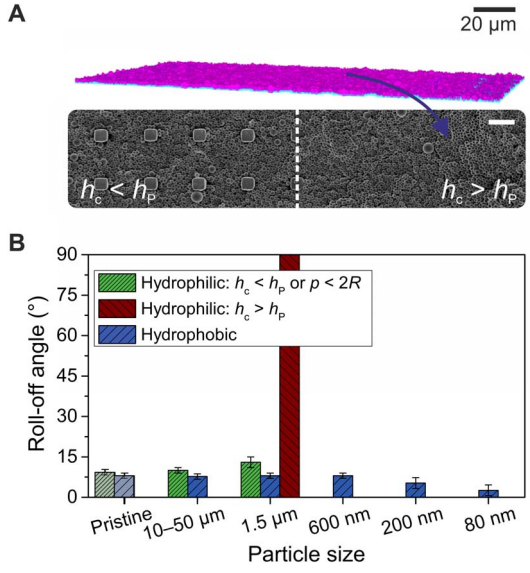

Fig. 4. Contamination and self-cleaning of superhydrophobic microstructured SU-8 pillars (rectangular, 10-μm height with 5 × 5–μm² top areas; center-center distance of pillars, 20 μm). (**A**) LSCM (top) and SEM (bottom) images showing a surface contaminated with 1.5-μm particles. On the left side of the SEM image, the micropillar array is only partially filled with particles ($h_c < h_P$), whereas on the right, the particles completely covered the microstructure ($h_c > h_P$). Scale bar, 10 μm (SEM). (**B**) Roll-off angles of 6-μl water drops after contamination of the micropillar array with hydrophilic and hydrophobic particles of various sizes and subsequent self-cleaning.

over the contaminated surface, individual particles were picked up at the advancing contact line (Fig. 5A, top). Upon further movement of the drop, these particles accumulated at the lower air-water interface of the drop (Fig. 5A, center). The drop rested on these hydrophilic particles. The air-water-particle contact lines were pinned at the lower side of the hydrophilic particles and showed contact angles of θ ≈ 40° to 50° (Fig. 5B). Thus, the particles acted as reentrant structures (*34*–*37*) supporting the weight of the droplet and preventing the droplet from contacting the surface. At the receding side, the drop lifted the particles from the surface, yielding a layer of particles on the drop, and a so-called liquid marble (*38*, *39*) formed (Fig. 5A, bottom). The same behavior was observed for the hydrophobic 10- to 50-μm particles (Fig. 5C and movie S2). However, the hydrophobic particles exhibited contact angles of θ ≈ 90° to 100°, and the water drop rested on the top half of the particles. The experiments with both hydrophilic and hydrophobic particles clearly showed an air gap underneath the drop. The gap distance H can be calculated using $H = R(1 - \cos\theta)$. For a sufficient number of large particles of $R \approx 20$ μm and a contact angle of 100°, we calculated $H \approx 24$ μm. This value is in good agreement with the confocal image (Fig. 5C). Smaller-sized particles were picked up similarly; however, the gap cannot be resolved by LSCM (movie S3).

Quantifying the forces during self-cleaning

To remove particles from a superhydrophobic surface, the capillary force F_C acting on the particle at the rear side of the drop needs to overcome the adhesion force between the particle and the surface, F_{Adh}. When the drop recedes and starts pulling on a particle that is adhering to the substrate at the bottom and to the air-water interface at the top side, the interface is deforming and a meniscus forms (Fig. 5D). The meniscus acts as a spring with spring constant k (*40*–*42*)

$$k \approx \frac{2\pi\gamma}{0.81 - \ln(R/l_C)} \quad (1)$$

and pulls on the particle with a capillary force $F_C = k\delta$. Here, δ is the deformation of the surface of the drop in normal direction, γ is the surface tension of water, R is the radius of the particle, and $l_C = \sqrt{\gamma/g\rho} = 2.7$ mm is the capillary length of water. The capillary force pulls on the particle until the adhesion force between the substrate and the particle is overcome, that is, for $F_C \geq F_{Adh}$. The adhesion force between a flat surface and a spherical particle can be estimated by the JKR (Johnson-Kendall-Roberts) theory (*43*)

$$F_{Adh} \approx \frac{3}{2}\pi R\varphi\Delta\gamma \quad (2)$$

Here, Δγ is the work of adhesion between the hydrophobic substrate and the particle surface (see the Supplementary Materials). We estimate it to be in the order of $\gamma = 0.11$ N m^{-1}. To take into account that superhydrophobic surfaces are rough and roughness greatly reduces the effective contact area between the particle and the surface, we added φ, which is the surface fraction in contact with the particle surface as compared with the apparent contact area. From SEM images, we estimate it to be $\varphi \approx 0.2$. The work to pick up a single particle W_s is given by the deformation δ of the air-water meniscus before the adhesion force is overcome (Fig. 5D)

$$W_s = \frac{1}{2}k\delta^2 = \frac{1}{2}k\frac{F_{Adh}^2}{k^2} = \frac{F_{Adh}^2}{2k} \quad (3)$$

When the drops move a distance Δx horizontally on the superhydrophobic surface, the work required is $\Delta W = wnW_s\Delta x$, accordingly. Here, n is the number of particles per unit area, and w is the width of the apparent contact area of the drop. Now, we can estimate the amount of the lateral adhesion force from

$$F_L = \frac{\Delta W}{\Delta x} = wnW_s = \frac{wnF_{Adh}^2}{2k} \quad (4)$$

We estimate the particle density to be approximately $0.1R^{-2}$. Thus, we can estimate the lateral force caused by the removal of particles from a surface

$$F_L \approx w\frac{1}{10R^2}\frac{1}{2k}\left[\frac{3}{2}\pi R\varphi\Delta\gamma\right]^2 = 1.1\frac{w\varphi^2\Delta\gamma^2}{k} \quad (5)$$

Here, we further neglected lateral interactions between particles and assumed that each particle is detached independent from its neighbor. With $w \approx 0.5$ mm and $k = 0.082$ N m^{-1} for $R = 25$ μm, the lateral adhesion force is $F_L \approx 3$ μN (see the Supplementary Materials for a more detailed discussion). This force can be compared to the force measured by our custom-built droplet adhesion force instrument (DAFI) (*44*). Here, a capillary drags a liquid drop over a surface (Fig. 5E), and the lateral adhesion force is measured using a force

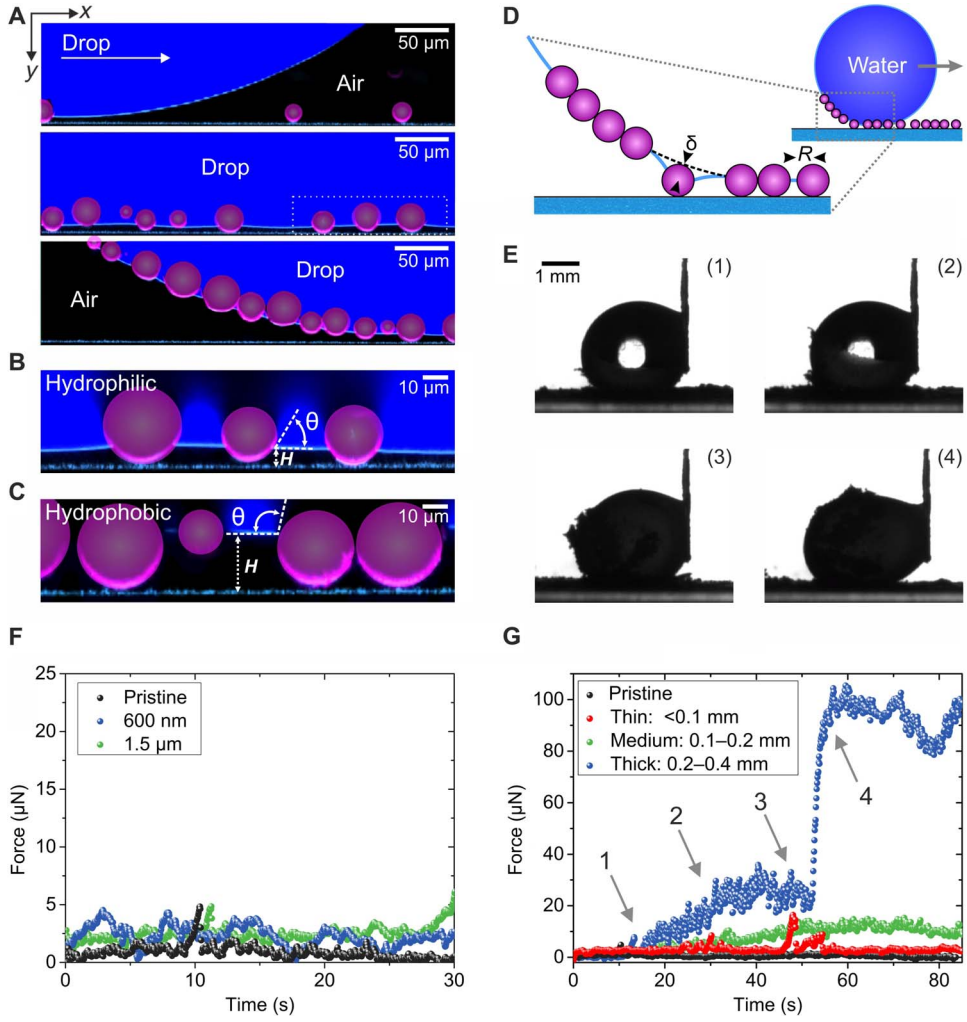

Fig. 5. Illustration of the self-cleaning of a contaminated superhydrophobic surface using confocal microscopy and friction force measurements. (**A**) A 10-μl water drop (dyed with ATTO 488; navy blue) is dragged over a nanoporous superhydrophobic surface contaminated with 10- to 50-μm hydrophilic particles (purple). The interface between the drop and the surface is monitored by LSCM. Particle contamination is completely taken along by the water drop (see Materials and Methods and fig. S9 for details of the image processing). (**B** and **C**) High-magnification LSCM images showing the contact angle θ of the hydrophilic and hydrophobic particles in contact with water. Smaller particles lost contact with the solid surface. (**D**) Sketch of the pickup process of particles. The deformed meniscus pulls on the particle. (**E**) Macroscopic observation of a 10-μl drop being dragged over a surface heavily contaminated with hydrophilic 10- to 50-μm particles. (**F**) Force required to clean a surface contaminated with hydrophilic 1.5-μm and 600-nm particles. The drop is moved at a velocity of v = 250 μm s^{-1}. (**G**) Effect of the thickness of the contamination layer (<0.1 mm, 0.1 to 0.2 mm, and 0.2 to 0.4 mm) for hydrophilic 10- to 50-μm particles on the force required to clean the surface. For strongly contaminated surfaces (0.2- to 0.4-mm contamination layer), a continuous increase in the force during the self-cleaning can be observed (1 and 2). Upon complete coverage of the drop's surface with particles (between 3 and 4), a sudden increase in force can be observed. Drop velocity, v = 250 μm s^{-1}.

sensor (see Materials and Methods for details). The force required to pick up a thin contamination layer (<50 μm) of hydrophilic particles using a 10-μl water drop ranged from 2 to 5 μN (Fig. 5F). Thus, the estimated values agree well with the experimental results. This agreement indicates that the model captures the essential process. Note that the lateral friction force only slightly exceeded the friction force on the pristine substrate (≈1 μN). The static lateral adhesion force is overcome when a drop starts rolling off a surface: $F_L = F_g = mg \sin\alpha$. Here, m = 10 mg is the mass of the water drop, and α is the roll-off angle. The friction force on slightly contaminated surfaces remained below 5 μN, corresponding to a roll-off angle ≤3°. These low roll-off angles demonstrate that the surfaces can be easily cleaned. The drops roll off the contaminated surface and simultaneously clean it.

Heavily contaminated surfaces

Whereas a thin layer of hydrophilic 10- to 50-μm particles (one to two layers of particles) can easily be removed from the surface, the force increased with an increasing contamination layer thickness (≈3 to 6 layers of particles; Fig. 5G, medium). For a thick contamination layer (≈8 to 12 layers), the force increased sharply to 100 μN at $t \approx 50$ s (Fig. 5G, thick). This increase corresponds to a travel distance of $s = vt = 1.3$ cm, for a drop velocity of v = 250 μm s^{-1}. Within this distance, the drop performed approximately 1.5 revolutions, as $2\pi R_{Drop} \approx$ 0.8 cm. After this distance, the drop is surrounded by a layer of particles and particle aggregates, as verified by video microscopy (Fig. 5E). The particles rapidly leave the contact area, trying to provide a homogeneous coverage of the surface. This proceeds until no more particles can be

taken up and leads to interfacial jamming. As soon as the drop is covered by a layer of particles, a liquid marble is formed. After that, the particle-loaded drop rolls over particles. This is associated with a force of 100 μN, which is 10 to 20 times higher than the lateral adhesion force for a drop only partially coated with particles (roll-off angle >90°). Thus, thick contamination layers may not be cleaned with a single drop. Consequently, the drop size needs to be increased, or several drops are required to clean the surface.

Real-world contamination

To compare the results based on model contamination to real-world outdoor exposure, we fixed several coated fabrics on a car. These so-termed superomniphobic fabrics repelled water and organic liquids and were chosen because of their robustness (*13*). They were obtained by coating polyester fabrics with the same nanostructured coating consisting of silicone nanofilaments. Fluorination renders the superhydrophobic fabrics superomniphobic (Fig. 6, A and B). Various liquids like water, coffee, wine, and hexadecane showed high receding contact angles and typically rolled off below 10°. The fabrics on the car were exposed to the atmosphere of the Rhineland-Palatine area in Germany for 257 days within a period of 426 days, covering all seasons and exposure to high ultraviolet radiation, rain, frost, and icing (temperatures ranged between −10 and 32°C, and humidities ranged between 40 and 100%; table S1 summarizes the temperatures, humidities, and rainfall during the exposure periods). This also included daily driving at velocities of 60 km hour^{-1} and maximal velocities on the highway of up to 140 km hour^{-1}. During this period, the owner drove more than 5000 km. The car was parked outside, i.e., not in a garage. The experiment started beginning of October 2016. The fabrics were fixed at the front window (A-pillar), side mirror, rear side window, and back window of the car (Fig. 6C and fig. S12).

Superomniphobic fabrics with slightly different wetting properties were used to account for variances in the fabrication of the surfaces. Therefore, we observed roll-off angles for water and hexadecane ranging between 2° and 4° and between 9° and 13° for 5-μl water and hexadecane drops, respectively (Fig. 6, D to G). Roll-off and receding contact

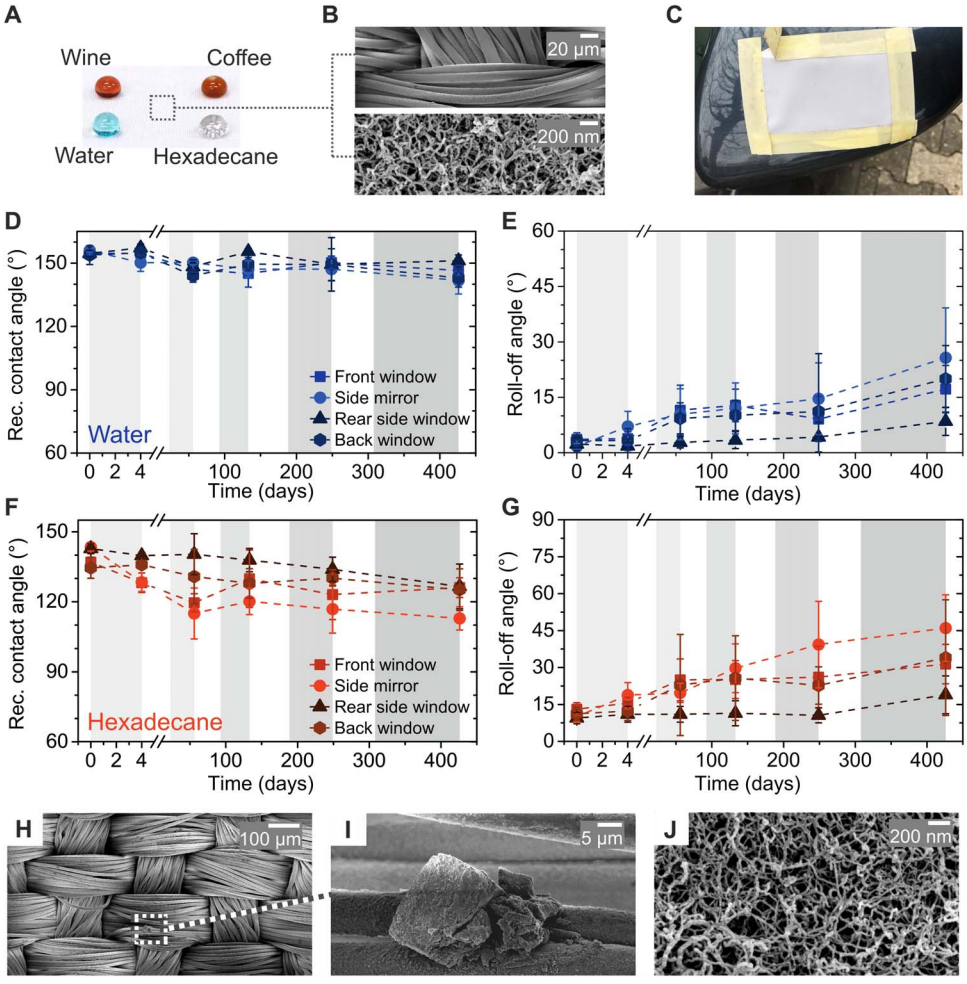

Fig. 6. Real-world contamination test through outdoor exposure of superomniphobic fabrics fixed on a car for 257 days. (**A**) Photograph of 20-μl drops of water (stained with methylene blue), coffee, wine, and hexadecane on a superomniphobic fabric. (**B**) SEM images of a coated superomniphobic polyester fabric at different magnifications. (**C**) Superomniphobic fabric fixed on the side mirror of the car. The fabric remained white even after 257 days of outdoor exposure. (**D** and **E**) Receding contact angles and roll-off angles of 5-μl water drops in the course of the outdoor exposure of 257 days within a period of 426 days. Periods of outdoor exposure are marked in gray. (**F** and **G**) Receding contact angles and roll-off angles of 5-μl hexadecane drops in the course of the outdoor exposure. Periods of outdoor exposure are marked in gray. (**H**) SEM image of a superomniphobic fabric after 257 days of outdoor exposure. (**I**) Higher-magnification SEM image of a dirt particle on a superomniphobic fabric. (**J**) High-magnification SEM image of the nanofilaments on a superomniphobic fabric after 257 days of outdoor exposure.

angles were measured after 4, 38, 79, 139, and 257 days of outdoor exposure. In between these days, the superomniphobic fabrics were removed, and the measurements were conducted. Even after 257 days of exposure, the roll-off angles stayed below 25° and 50° for water and hexadecane, respectively. The superomniphobic fabric fixed at the front of the side mirror experienced the most wear and contamination under the impact of insects and dirt. SEM analysis of the fabrics taken after 426 days without any further rinsing or cleaning showed only sparse particle contamination (in the 10-μm range) (Fig. 6, H and I). No nanocontamination between the nanofilaments could be detected (Fig. 6J). Likely, contamination was removed by morning dew or rain. For example, particles can dissolve in the water or stick to the air-water interface and roll off as soon as the dew drop can overcome the lateral adhesion force. Furthermore, the release of surface energy after coalescence of neighboring dew drops can cause merged drops to jump off the surface (*45*), taking particles along. In addition, rain periods contribute to the self-cleaning of the surfaces. Likely, the major part of the reduction in repellency properties was due to mechanical damages (fig. S13).

Industrial contamination test

The results of the tests mentioned above were further supplemented by an industrial dirt pickup simulation test for paints and coatings from Evonik Resource Efficiency GmbH (fig. S14). Here, superomniphobic fabrics and benchmarks were exposed to a dirt treatment inside an industrial dishwasher. The dirt simulation process and dirt mixture are adapted from a method described in European patent application EP1302765. Afterward, the surfaces were cleaned in a washing step by spraying distilled water. The whole procedure lasted 3 hours, which effectively corresponds to 18 months of outdoor exposure. Last, the change in whiteness ΔL was measured. The superomniphobic fabrics retained their whiteness, showing only a minor change of $\Delta L = 8 \pm 1$ (fig. S14C). In comparison, an untreated fabric showed $\Delta L = 59$, and benchmark surfaces range between 30 and 40. The differences can be explained by the small pore size of the nanofilaments, resulting in self-cleaning and high resistance of the superomniphobic fabrics toward contamination compared with the bare fabrics and benchmark surfaces.

CONCLUSION

During self-cleaning, particulate contaminations are lifted at the receding contact line. Therefore, the friction force is determined by the adhesion force of the individual particles to the superhydrophobic substrate. The forces can be quantified using a DAFI, allowing an in situ measurement of the forces during the self-cleaning process. Notably, the force required to clean a moderately contaminated surface is not substantially higher than the friction force the drop experiences when rolling over a pristine surface. Independent of the particles' size, the adhesion force of millimeter-sized drops remains below 5 μN for few contamination layers. Therefore, drops can pick up particulate contamination as soon as they are set into motion by slightly tilting the surface. However, the friction force increases by more than one order of magnitude when the drop is covered with particles, i.e., a liquid marble is formed. Consequently, additional drops are required to clean the surface.

The resistance of superhydrophobic surfaces to various kinds of particulate contamination is paramount since many applications rely on robust self-cleaning properties. Surfaces based on nanofilaments having a pore size below 500 nm withstand most kinds of particulate contamination. This includes hydrophobic nanoparticle powders of various particle sizes as well as hydrophilic particles dispersed in ethanol down to around 600 nm in diameter. In environments with high nanoparticle pollutions of even smaller diameter, the pore size may be further lowered depending on the needs to provide an optimal endurance of the surface. Therefore, the pore size is the most important factor to achieve a high contamination resistance and should be designed as small as possible. In a real-word and industrial testing scenario, the small pore size of the nanofilament coating enabled it to remain mostly intact after severe and prolonged periods of exposure. This demonstrates that well-designed superhydrophobic and superomniphobic surfaces can resist real contamination scenarios.

MATERIALS AND METHODS

Materials

If not stated otherwise, experiments were carried out at room temperature. The following chemicals were used: TCMS (99%; Sigma-Aldrich), 1*H*,1*H*,2*H*,2*H*-perfluorodecyltrichlorosilane (PFDTS; 96%; Alfa Aesar), tetraethoxysilane (98%; Sigma-Aldrich), octyltrichlorosilane (97%; Sigma-Aldrich), (3-amino-propyl)triethoxysilane (98%; Sigma-Aldrich), iron(II) sulfate heptahydrate (>99%; Sigma-Aldrich), styrene (99%; stabilized; Acros Organics), acrylic acid (99.5%; Acros Organics), ammonium persulfate (98%; Acros Organics), sodium chloride (99.8%; Riedel-de Haën), sodium hydroxide (98%; Sigma-Aldrich), ammonia (25%; VWR Chemicals), hydrogen peroxide (35 weight %, VWR Chemicals), SU-8 3010 photoresist (MicroChem), mr-Dev 600 developer (Micro Resist Technology), *n*-hexane (99.99%; Fisher Chemical), toluene (99.99%; Fisher Chemical), *m*-xylene (98%; Sigma-Aldrich), isopropanol (99.5%; Fisher Chemical), ethanol (absolute; 99.96%; VWR Chemicals), hexadecane (99%; Sigma-Aldrich), methylene blue (>82%; Sigma-Aldrich), rhodamine B isothiocyanate (mixed isomers; Sigma-Aldrich), Nile red (Sigma-Aldrich), and ATTO 488 (ATTO-TEC). Reagents were used as received. Wine and coffee were purchased from the local supermarket. Polyester fabrics (76 g m^{-2}; weave "Crêpe de chine") were obtained from Karstadt. Glass beads (10 to 50 μm) were obtained from Duke Scientific Corp. Glass slides of 24 × 60 mm^2 and a thickness of 150 ± 5 μm were obtained from Menzel-Gläser. Purified Milli-Q water from Sartorius Arium Pro VF was used for all experiments.

Preparation of the superhydrophobic glass slides

The nanoporous superhydrophobic glass slides were prepared as previously reported (*7*, *13*, *46*). Typically, glass slides were plasma cleaned and activated in an oxygen plasma chamber (Diener Electronic Femto; 120 W, 5 min, 6 cm^3 min^{-1} oxygen flow rate). TCMS was mixed with toluene having a water content of 180 ± 10 ppm (parts per million) (400 μl of TCMS per 100 ml of toluene). The water content was evaluated using a Karl Fischer coulometer (METTLER TOLEDO C20 Compact KF coulometer). The solution was stirred for 60 s. Afterward, the activated glass slides were immersed in the solution, and the reaction chamber was sealed. After 6 hours, the TCMS-coated glass slides were rinsed with *n*-hexane and dried under a nitrogen stream. To modify the TCMS-coated glass slides with PFDTS, they were activated in an oxygen plasma chamber (Diener Electronic Femto; 120 W, 2 min, 7 cm^3 min^{-1} oxygen flow rate). Subsequently, 50 μl of PFDTS was mixed with 100 ml of *n*-hexane. The activated substrates were immersed in the solution for 20 min, rinsed with *n*-hexane, and dried under a nitrogen stream.

Preparation of the superomniphobic fabrics

The superomniphobic fabrics were prepared as previously reported (*13*). Polyester fabrics were cleaned by ultrasonication in ethanol.

The dried polyester fabrics were coated with nanofilaments by adding 1400 µl of TCMS to a reaction chamber containing 350 ml of toluene with a water content of 150 to 160 ppm. The water content was evaluated using a Karl Fischer coulometer (METTLER TOLEDO C20 Compact KF coulometer). The solution was stirred for 60 s. Afterward, fabrics were immersed in the solution, and the reaction chamber was sealed. After 3 hours, the TCMS-coated fabrics were rinsed with *n*-hexane and dried under a nitrogen stream. To modify the TCMS-coated fabrics with PFDTS, they were activated in an oxygen plasma chamber (Diener Electronic Femto; 120 W, 2 min, 7 cm^3 min^{-1} oxygen flow rate). Subsequently, 180 µl of PFDTS was mixed with 350 ml of *n*-hexane. The activated substrates were immersed in the solution for 20 min, rinsed with *n*-hexane, and dried under a nitrogen stream.

Superhydrophobic SU-8 micropillars

SU-8 micropillar arrays were prepared on glass slides by photolithography as previously reported (*44*, *47*). The rectangular pillars were designed 10 µm high with 5 × 5–$µm^2$ top areas. The pillar-pillar distance between the centers of two adjacent pillars in a row was 20 µm. The SU-8 micropillars were activated in an oxygen plasma chamber (Diener Electronic Femto; 30 W, 2 min, 6 cm^3 min^{-1} oxygen flow rate). Subsequently, PFDTS was mixed with *n*-hexane (50 µl of PFDTS per 100 ml of *n*-hexane). The activated SU-8 micropillar–coated glass slides were immersed in the solution, and the reaction chamber was sealed. After 20 min, the fluorinated pillars were rinsed with *n*-hexane and dried under a nitrogen stream.

Contamination experiments

To contaminate the superhydrophobic surfaces with hydrophobic particle powders, ≈10 mg of the dried particle powder was distributed on an area of ≈1 cm^2. To contaminate the superhydrophobic surfaces with hydrophilic particles, 50 to 100 µl of 10 g $liter^{-1}$ dispersions of the particles in ethanol was slowly pipetted onto the surface. The dispersion was dried under ambient atmosphere at room temperature. Afterward, the contamination was cleaned by placing 20 to 50 water drops (16 ± 1 µl) on the inclined surface. The first few drops (<10) removed the most visible contamination. However, to ensure that all contamination that can be cleaned by water drops was removed, an excess number of drops was used.

Laser scanning confocal microscopy

LSCM images were taken using an inverted confocal microscope (Leica TCS SP8 SMD, HCX PL APO 40×/0.85 CORR CS dry objective) using the Leica LAS X software. The surfaces were contaminated as described in the section on "Contamination experiments." LSCM images were taken before and after cleaning. For the visualization of the self-cleaning process, 10-µl water drops (dyed with ATTO 488, 1 mg $liter^{-1}$) were placed onto sparsely contaminated superhydrophobic nanoporous glass slides. The drops were slowly dragged over the surface using a metal needle (0.26-mm outer diameter, 31 gauge) attached on a stage similar to the droplet adhesion force measurements. The self-cleaning process was recorded using the LSCM. The fluorescence of ATTO 488 in water and the fluorescence of the dyed particles were shown in navy blue and pink, respectively. The reflection of light was shown in light blue. Reflection and fluorescence signals were recorded simultaneously.

Processing of laser scanning confocal microscopy images

The LSCM images in Fig. 5 were processed according to the procedure illustrated in fig. S9. For the creation of the three-dimensional (3D) LSCM images, the Leica LAS X (3D viewer) software was used. Intensities of the reflection and fluorescence channels were adjusted for best clarity. In Figs. 2C and 3C, particle illustrations were added as described in fig. S9 (A and B).

Contact angle measurements

Static contact angles were measured using a DataPhysics OCA 35 contact angle goniometer. Drops 6 µl in size were deposited onto the substrate. The measurement was repeated in three different spots per substrate. The error of the static contact angle measurements was estimated to be between ±4° and ±8°, depending on the substrate.

For advancing and receding contact angles, 6-µl drops were deposited on the surface. Afterward, 20 µl of the liquid was added to and removed from the drop. The measurement was consecutively repeated three times at the same spot and at three different spots per substrate. The error of the advancing and receding contact angle measurements was estimated to be ±4°.

Roll-off angles were measured using the DataPhysics OCA 35 contact angle goniometer. Therefore, 6-µl drops (6 µl for nanofilament-coated glass slides and 5 µl for nanofilament-coated fabrics) were deposited on the substrates, and the measuring plate was tilted until the drops rolled off. The roll-off angle was determined in at least six different spots per substrate, and mean roll-off angles and corresponding SDs were calculated.

DAFI experiments

Droplet adhesion force experiments were conducted with a custom-built setup similar to that in (*44*). A glass capillary was coupled to a force sensor [FTS-1000, FemtoTools; instead of the laser and position sensitive detector (PSD) (*44*)]. The sensor had a resolution in the range of a single micronewton and a time resolution of 1 kHz. To measure the lateral adhesion force, a drop was deposited on a substrate, and the drop was approached using the glass capillary. The substrate movement was realized using a linear stage with a customized stepper motor and gear set. The measurements were conducted at a speed of 250 µm s^{-1}.

Scanning electron microscopy

SEM images were taken with a Zeiss LEO 1530 Gemini SEM at gun voltages of 3 kV using the in-lens detector. To avoid charging, samples were sputtered with Pt before measurement using a Bal-Tec MED 020 modular high vacuum coating system (with an argon pressure of 2 × 10^{-5} bar and a current of 30 mA, 7-nm Pt).

SUPPLEMENTARY MATERIALS

Supplementary material for this article is available at http://advances.sciencemag.org/cgi/content/full/6/3/eaaw9727/DC1

Supplementary Materials and Methods

Fig. S1. SEM images of the model contamination particles.

Fig. S2. LSCM images of nanoporous surfaces contaminated with hydrophobic particle powder.

Fig. S3. SEM images of a nanoporous surface after contamination with hydrophobic 80-nm particles.

Fig. S4. LSCM images of nanoporous surfaces contaminated with hydrophilic particles from ethanol dispersion.

Fig. S5. SEM images of a nanoporous surface after contamination with a thin layer of hydrophilic 600-nm particles.

Fig. S6. Coffee stain effect during evaporation.

Fig. S7. SEM images of nanoporous surfaces after contamination with hydrophilic 200- and 80-nm particles.

Fig. S8. Water droplet on a nanoporous surface contaminated with nanoparticles.

Fig. S9. Processing of the LSCM images.

Fig. S10. Contamination and self-cleaning of superhydrophobic microstructured SU-8 pillars.

Fig. S11. SEM images of superhydrophobic microstructured SU-8 pillars after contamination with hydrophobic particles.
Fig. S12. Photographs of the superomniphobic fabrics on the car after 257 days of outdoor exposure.
Fig. S13. SEM images of abraded microfibers.
Fig. S14. Industrial contamination test.
Table S1. Temperatures (*T*) and rainfall and humidities (RH) during the outdoor exposure of the superomniphobic fabrics.
Movie S1. Self-cleaning process of hydrophilic 10- to 50-μm particles.
Movie S2. Self-cleaning process of hydrophobic 10- to 50-μm particles.
Movie S3. Self-cleaning process of hydrophilic 1.5-μm particles.
Note S1. Imaging self-cleaning.
References (*48*–*59*)

REFERENCES AND NOTES

1. U. Pöschl, Atmospheric aerosols: Composition, transformation, climate and health effects. *Angew. Chem. Int. Ed.* **44**, 7520–7540 (2005).
2. W. Barthlott, C. Neinhuis, Purity of the sacred lotus, or escape from contamination in biological surfaces. *Planta* **202**, 1–8 (1997).
3. B. Deng, R. Cai, Y. Yu, H. Jiang, C. Wang, J. Li, L. Li, M. Yu, J. Li, L. Xie, Q. Huang, C. Fan, Laundering durability of superhydrophobic cotton fabric. *Adv. Mater.* **22**, 5473–5477 (2010).
4. J. Zhang, S. Seeger, Polyester materials with superwetting silicone nanofilaments for oil/water separation and selective oil absorption. *Adv. Funct. Mater.* **21**, 4699–4704 (2011).
5. B. J. Privett, J. Youn, S. A. Hong, J. Lee, J. Han, J. H. Shin, M. H. Schoenfisch, Antibacterial fluorinated silica colloid superhydrophobic surfaces. *Langmuir* **27**, 9597–9601 (2011).
6. T. Darmanin, F. Guittard, Recent advances in the potential applications of bioinspired superhydrophobic materials. *J. Mater. Chem. A* **2**, 16319–16359 (2014).
7. F. Geyer, M. D'Acunzi, C.-Y. Yang, M. Müller, P. Baumli, A. Kaltbeitzel, V. Mailänder, N. Encinas, D. Vollmer, H.-J. Butt, How to coat the inside of narrow and long tubes with a super-liquid-repellent layer—A promising candidate for antibacterial catheters. *Adv. Mater.* **31**, e1801324 (2018).
8. N. J. Shirtcliffe, G. McHale, M. I. Newton, Y. Zhang, Superhydrophobic copper tubes with possible flow enhancement and drag reduction. *ACS Appl. Mater. Interfaces* **1**, 1316–1323 (2009).
9. B. Bhushan, Y. C. Jung, Natural and biomimetic artificial surfaces for superhydrophobicity, self-cleaning, low adhesion, and drag reduction. *Prog. Mater. Sci.* **56**, 1–108 (2011).
10. L. Cao, A. K. Jones, V. K. Sikka, J. Wu, D. Gao, Anti-icing superhydrophobic coatings. *Langmuir* **25**, 12444–12448 (2009).
11. L. Mishchenko, B. Hatton, V. Bahadur, J. A. Taylor, T. Krupenkin, J. Aizenberg, Design of ice-free nanostructured surfaces based on repulsion of impacting water droplets. *ACS Nano* **4**, 7699–7707 (2010).
12. M. Paven, P. Papadopoulos, S. Schöttler, X. Deng, V. Mailänder, D. Vollmer, H.-J. Butt, Super liquid-repellent gas membranes for carbon dioxide capture and heart–lung machines. *Nat. Commun.* **4**, 2512 (2013).
13. F. Geyer, C. Schönecker, H.-J. Butt, D. Vollmer, Enhancing CO_2 capture using robust superomniphobic membranes. *Adv. Mater.* **29**, 1603524 (2017).
14. L. Feng, Z. Zhang, Z. Mai, Y. Ma, B. Liu, L. Jiang, D. Zhu, A super-hydrophobic and super-oleophilic coating mesh film for the separation of oil and water. *Angew. Chem. Int. Ed.* **43**, 2012–2014 (2004).
15. Y. Liao, R. Wang, A. G. Fane, Engineering superhydrophobic surface on poly(vinylidene fluoride) nanofiber membranes for direct contact membrane distillation. *J. Memb. Sci.* **440**, 77–87 (2013).
16. A. Razmjou, E. Arifin, G. Dong, J. Mansouri, V. Chen, Superhydrophobic modification of TiO_2 nanocomposite PVDF membranes for applications in membrane distillation. *J. Membr. Sci.* **415–416**, 850–863 (2012).
17. R. P. Garrod, L. G. Harris, W. C. Schofield, J. McGettrick, L. J. Ward, D. O. Teare, J. P. Badyal, Mimicking a stenocara beetle's back for microcondensation using plasmachemical patterned superhydrophobic–superhydrophilic surfaces. *Langmuir* **23**, 689–693 (2006).
18. K.-C. Park, S. S. Chhatre, S. Srinivasan, R. E. Cohen, G. H. McKinley, Optimal design of permeable fiber network structures for fog harvesting. *Langmuir* **29**, 13269–13277 (2013).
19. A. Lafuma, D. Quéré, Superhydrophobic states. *Nat. Mater.* **2**, 457–460 (2003).
20. A. B. D. Cassie, S. Baxter, Wettability of porous surfaces. *Trans. Faraday Soc.* **40**, 546–551 (1944).
21. R. Fürstner, W. Barthlott, C. Neinhuis, P. Walzel, Wetting and self-cleaning properties of artificial superhydrophobic surfaces. *Langmuir* **21**, 956–961 (2005).
22. B. Bhushan, Y. C. Jung, K. Koch, Self-cleaning efficiency of artificial superhydrophobic surfaces. *Langmuir* **25**, 3240–3248 (2009).
23. Y.-B. Park, H. Im, M. Im, Y.-K. Choi, Self-cleaning effect of highly water-repellent microshell structures for solar cell applications. *J. Mater. Chem.* **21**, 633–636 (2011).
24. K. M. Wisdom, J. A. Watson, X. Qu, F. Liu, G. S. Watson, C.-H. Chen, Self-cleaning of superhydrophobic surfaces by self-propelled jumping condensate. *Proc. Natl. Acad. Sci. U.S.A.* **110**, 7992–7997 (2013).
25. M. Jönsson-Niedziółka, F. Lapierre, Y. Coffinier, S. J. Parry, F. Zoueshtiagh, T. Foat, V. Thomy, R. Boukherroub, EWOD driven cleaning of bioparticles on hydrophobic and superhydrophobic surfaces. *Lab Chip* **11**, 490–496 (2011).
26. F. Schellenberger, N. Encinas, D. Vollmer, H.-J. Butt, How water advances on superhydrophobic surfaces. *Phys. Rev. Lett.* **116**, 096101 (2016).
27. G. R. J. Artus, S. Jung, J. Zimmermann, H.-P. Gautschi, K. Marquardt, S. Seeger, Silicone nanofilaments and their application as superhydrophobic coatings. *Adv. Mater.* **18**, 2758–2762 (2006).
28. J. Zhang, S. Seeger, Superoleophobic coatings with ultralow sliding angles based on silicone nanofilaments. *Angew. Chem. Int. Ed.* **50**, 6652–6656 (2011).
29. P. Saxena, L. M. Hildemann, Water-soluble organics in atmospheric particles: A critical review of the literature and application of thermodynamics to identify candidate compounds. *J. Atmos. Chem.* **24**, 57–109 (1996).
30. A. P. Sullivan, R. J. Weber, A. L. Clements, J. R. Turner, M. S. Bae, J. J. Schauer, A method for on-line measurement of water-soluble organic carbon in ambient aerosol particles: Results from an urban site. *Geophys. Res. Lett.* **31**, L13105 (2004).
31. R. D. Deegan, O. Bakajin, T. F. Dupont, G. Huber, S. R. Nagel, T. A. Witten, Capillary flow as the cause of ring stains from dried liquid drops. *Nature* **389**, 827–829 (1997).
32. H. J. Butt, M. Kappl, *Surface and Interfacial Forces* (Wiley-VCH, 2010).
33. L. Mammen, K. Bley, P. Papadopoulos, F. Schellenberger, N. Encinas, H.-J. Butt, C. K. Weiss, D. Vollmer, Functional superhydrophobic surfaces made of Janus micropillars. *Soft Matter* **11**, 506–515 (2014).
34. A. Tuteja, W. Choi, M. Ma, J. M. Mabry, S. A. Mazzella, G. C. Rutledge, G. H. McKinley, R. E. Cohen, Designing superoleophobic surfaces. *Science* **318**, 1618–1622 (2007).
35. T. Liu, C.-J. Kim, Turning a surface superrepellent even to completely wetting liquids. *Science* **346**, 1096–1100 (2014).
36. J. Li, X. Zhou, J. Li, L. Che, J. Yao, G. McHale, M. K. Chaudhury, Z. Wang, Topological liquid diode. *Sci. Adv.* **3**, eaao3530 (2017).
37. E. M. Domingues, S. Arunachalam, J. Nauruzbayeva, H. Mishra, Biomimetic coating-free surfaces for long-term entrapment of air under wetting liquids. *Nat. Commun.* **9**, 3606 (2018).
38. P. Aussillous, D. Quéré, Liquid marbles. *Nature* **411**, 924–927 (2001).
39. S. Fujii, S.-i. Yusa, Y. Nakamura, Stimuli-responsive liquid marbles: Controlling structure, shape, stability, and motion. *Adv. Funct. Mater.* **26**, 7206–7223 (2016).
40. O. Pitois, X. Chateau, Small particle at a fluid interface: Effect of contact angle hysteresis on force and work of detachment. *Langmuir* **18**, 9751–9756 (2002).
41. H.-J. Butt, N. Gao, P. Papadopoulos, W. Steffen, M. Kappl, R. Berger, Energy dissipation of moving drops on superhydrophobic and superoleophobic surfaces. *Langmuir* **33**, 107–116 (2016).
42. Y. Tang, S. Cheng, Capillary forces on a small particle at a liquid-vapor interface: Theory and simulation. *Phys. Rev. E* **98**, 032802 (2018).
43. K. L. Johnson, K. Kendall, A. D. Roberts, Surface energy and the contact of elastic solids. *Proc. R. Soc. A* **324**, 301–313 (1971).
44. N. Gao, F. Geyer, D. W. Pilat, S. Wooh, D. Vollmer, H.-J. Butt, R. Berger, How drops start sliding over solid surfaces. *Nat. Phys.* **14**, 191–196 (2018).
45. J. B. Boreyko, C.-H. Chen, Self-propelled dropwise condensate on superhydrophobic surfaces. *Phys. Rev. Lett.* **103**, 184501 (2009).
46. C. Shi, X. Cui, X. Zhang, P. Tchoukov, Q. Liu, N. Encinas, M. Paven, F. Geyer, D. Vollmer, Z. Xu, H.-J. Butt, H. Zeng, Interaction between air bubbles and superhydrophobic surfaces in aqueous solutions. *Langmuir* **31**, 7317–7327 (2015).
47. P. Papadopoulos, L. Mammen, X. Deng, D. Vollmer, H.-J. Butt, How superhydrophobicity breaks down. *Proc. Natl. Acad. Sci. U.S.A.* **110**, 3254–3258 (2013).
48. M. D'Acunzi, Core-shell particles and their application for superhydrophobic surfaces, thesis, Johannes Gutenberg-Universität, Mainz (2010).
49. N. A. M. Verhaegh, A. van Blaaderen, Dispersions of rhodamine-labeled silica spheres: Synthesis, characterization, and fluorescence confocal scanning laser microscopy. *Langmuir* **10**, 1427–1438 (1994).
50. H. J. H. Fenton, LXXIII.—Oxidation of tartaric acid in presence of iron. *J. Chem. Soc. Trans.* **65**, 899–910 (1894).
51. J. J. Pignatello, E. Oliveros, A. MacKay, Advanced oxidation processes for organic contaminant destruction based on the fenton reaction and related chemistry. *Crit. Rev. Environ. Sci. Technol.* **36**, 1–84 (2006).
52. L. Zhang, M. D'Acunzi, M. Kappl, G. K. Auernhammer, D. Vollmer, C. M. van Kats, A. van Blaaderen, Hollow silica spheres: Synthesis and mechanical properties. *Langmuir* **25**, 2711–2717 (2009).
53. W. Schaertl, H. Sillescu, Dynamics of colloidal hard spheres in thin aqueous suspension layers—Particle tracking by digital image processing and brownian dynamics computer simulations. *J. Colloid Interface Sci.* **155**, 313–318 (1993).

54. C. Huh, S. G. Mason, Sphere tensiometry: An evaluation and critique. *Can. J. Chem.* **54**, 969–978 (1976).
55. E. Bayramli, C. Huh, S. G. Mason, Sphere tensiometry: Wall effects and correction factors. *Can. J. Chem.* **56**, 818–823 (1978).
56. O. D. Velev, K. Furusawa, K. Nagayama, Assembly of latex particles by using emulsion droplets as templates. 1. Microstructured hollow spheres. *Langmuir* **12**, 2374–2384 (1996).
57. S. E. Anachkov, I. Lesov, M. Zanini, P. A. Kralchevsky, N. D. Denkov, L. Isa, Particle detachment from fluid interfaces: Theory vs. experiments. *Soft Matter* **12**, 7632–7643 (2016).
58. H. H. Kausch, D. G. Fesko, N. W. Tschoegl, The random packing of circles in a plane. *J. Colloid Interface Sci.* **37**, 603–611 (1971).
59. X. Zhang, Y. Guo, Z. Zhang, P. Zhang, Self-cleaning superhydrophobic surface based on titanium dioxide nanowires combined with polydimethylsiloxane. *Appl. Surf. Sci.* **284**, 319–323 (2013).

Acknowledgments: D. Vollmer provided a car for the outdoor experiments. We thank W. S. Y. Wong for carefully reading the manuscript. We thank S. Krusenbaum, G. Glasser, and G. Schäfer for technical support. **Funding:** This work was supported by the ERC Advanced Grant no. 340391 "SUPRO" (H.-J.B., D.V., and F.G.), the German Research Foundation (DFG) with the Collaborative Research Center 1194 (H.-J.B. and F.G.), the European Union's Horizon 2020 research and innovation program LubISS no. 722497 (D.V.). **Author contributions:** F.G. fabricated the surfaces, carried out the experiments and characterization unless stated otherwise below, and wrote the manuscript. M.D. prepared the nano- and microparticles. A.S., F.G., and N.G. carried out the lateral adhesion force experiments. A.S.-A. fabricated and characterized the superomniphobic fabrics for the outdoor exposure experiments. A.K. assisted in the laser scanning confocal measurements. T.-F.S. was responsible for the dirt dishwasher experiments. H.-J.B. and D.V. devised the theoretical calculation of the lateral adhesion force. F.G., D.V., R.B., and H.-J.B. contributed to the experimental planning, data analysis, and manuscript preparation. All authors reviewed and approved the manuscript. **Competing interests:** The authors declare that they have no competing interests. **Data and materials availability:** All data needed to evaluate the conclusions in the paper are present in the paper and/or the Supplementary Materials. Additional data related to this paper may be requested from the authors.

Submitted 14 February 2019
Accepted 13 September 2019
Published 17 January 2020
10.1126/sciadv.aaw9727

Citation: F. Geyer, M. D'Acunzi, A. Sharifi-Aghili, A. Saal, N. Gao, A. Kaltbeitzel, T.-F. Sloot, R. Berger, H.-J. Butt, D. Vollmer, When and how self-cleaning of superhydrophobic surfaces works. *Sci. Adv.* **6**, eaaw9727 (2020).

Science Advances

When and how self-cleaning of superhydrophobic surfaces works

Florian Geyer, Maria D'Acunzi, Azadeh Sharifi-Aghili, Alexander Saal, Nan Gao, Anke Kaltbeitzel, Tim-Frederik Sloot, Rüdiger Berger, Hans-Jürgen Butt and Doris Vollmer

Sci Adv **6** (3), eaaw9727.
DOI: 10.1126/sciadv.aaw9727

Science Advances (ISSN 2375-2548) is published by the American Association for the Advancement of Science, 1200 New York Avenue NW, Washington, DC 20005. The title *Science Advances* is a registered trademark of AAAS.